Chemical Engineering Journal 523 (2025) 168338

Contents lists available at ScienceDirect

Chemical Engineering Journal

journal homepage: www.elsevier.com/locate/cej

RNA hydrogel-based domino-like cascade reactor to enhance cancer therapy

Xiaofan Liu [a], Yun Yin [a], Jiajia Zhu [a], Ziyang Song [a], Weicai Wang [a,b], Xuemei Li [a,*], Huangxian Ju [b,*]

[a] Collaborative Innovation Center of Tumor Marker Detection Technology, Equipment and Diagnosis-Therapy Integration in Universities of Shandong, Shandong Province Key Laboratory of Detection Technology for Tumor Makers, School of Chemistry and Chemical Engineering, Linyi University, Linyi, 276005, China
[b] State Key Laboratory of Analytical Chemistry for Life Science, School of Chemistry and Chemical Engineering, Nanjing University, Nanjing, 210023, China

ARTICLE INFO

Keywords:
RNA hydrogel
Tumor microenvironment reprogramming
Synergistic therapy
MCT4
HIF-1α

ABSTRACT

The dynamic interactions and adaptive regulation between tumor cells and the tumor microenvironment (TME) contribute to the limited success of monotherapeutic approaches. In this study, we propose a domino-like cascade reactor (RCT-AC@$SnFe_2O_4$) based on RNA hydrogel. By designing a rolling circle template sequence encoding monocarboxylate transporter 4 small interfering RNA (MCT4 siRNA) and microRNA-199a (miR-199a), an RNA hydrogel carrier has been synthesized to load chlorin e6 (Ce6) and nanozymes ($SnFe_2O_4$) for potentiating anticancer efficacy. Upon exposure to intracellular dicer enzyme, the nanozymes and nucleic acid fragments within the reactor are released. The photothermal effect of the $SnFe_2O_4$ not only enables photothermal therapy (PTT) but also accelerates the decomposition of the RNA hydrogel. The released MCT4 siRNA silences MCT4 expression, which induces tumor cell acidification and upregulating peroxisome proliferator-activated receptor γ coactivator-1α (PGC1α) in mitochondria. This cascade reactions trigger substantial H_2O_2 generation to potentiate the Fenton-like reaction mediated by $SnFe_2O_4$ for amplified chemodynamic efficacy (CDT). Remarkably, the reactor depletes glutathione (GSH) to reduce tumor antioxidant capacity and amplify CDT efficiency. Concurrently, miR-199a released from the reactor suppresses hypoxia-inducible factor 1-α (HIF-1α), and elevates intracellular oxygen level, thereby enhancing Ce6-mediated photodynamic therapy (PDT). In vitro and in vivo experiments have demonstrated a gene-facilitated "PDT-CDT-PTT" cooperative mechanism of this reactor, showing significant potential for cancer therapy.

1. Introduction

Photodynamic therapy (PDT) and chemodynamic therapy (CDT) have emerged as promising non-invasive strategies for precision oncology, and their efficacy is severely constrained by the immunosuppressive and antioxidant tumor microenvironment (TME) [1–4]. Hypoxia impedes oxygen-dependent generation of cytotoxic singlet oxygen ($^1O_2$) in PDT, while insufficient endogenous hydrogen peroxide (H_2O_2) and glutathione (GSH) overexpression jointly suppress Fenton reaction-mediated hydroxyl radical (·OH) production in CDT [5–8]. The current lack of intelligent delivery systems capable of spatiotemporally coordinating multiple therapeutic agents has emerged as a critical hinder limiting the efficacy of synergistic therapies.

In recent years, researchers have attempted to integrate PDT, CDT, and photothermal therapy (PTT) to amplify oxidative stress and overcome the TME barrier. For instance, metal-organic frameworks (MOFs) and mesoporous silica nanoparticles (MSNs) have been engineered to co-load photosensitizers and chemotherapy drugs [9–13]. However, these rigid carriers often suffer from premature drug leakage, poor biodegradability, and an inability to dynamically regulate enzyme activity or deliver genetic payloads. What's more, multi-module synergies are still subject to key mechanism obstacles, nanozyme is prone to aggregation deactivation due to high surface energy [14–16], and the existing systems lack spatiotemporal specificity active oxygen species (ROS) strategy [17–19], which make it difficult to form dynamic matching between different treatment modes in the three dimensions of action site, timing, and dose [20]. How to accurately coordinate the spatio-temporal effects of different treatment modules and optimize their collaborative mechanisms are still facing challenges.

With sequence programmability, intelligent responsiveness and

* Corresponding authors.
E-mail addresses: xuemei_li@yeah.net (X. Li), hxju@nju.edu.cn (H. Ju).

https://doi.org/10.1016/j.cej.2025.168338
Received 30 May 2025; Received in revised form 8 September 2025; Accepted 9 September 2025
Available online 10 September 2025

excellent biocompatibility, nucleic acid hydrogels provide an ideal platform for multimodal therapeutic delivery [21–25]. The rotatable polymer chains within these hydrogels ensure structural flexibility, enabling precise co-encapsulation of photosensitizers [26,27], nanozymes [28,29], chemotherapeutic agents [30,31], and gene regulators [32,33], coupled with environmentally responsive degradation for on-demand payload release [34]. Through sequence-specific design, these hydrogels can achieve cellular/tissue-targeted delivery, enhancing therapeutic precision and efficacy [35–37]. Notably, monotherapy relying solely on nucleic acid delivery suffers from protracted treatment cycles, severely limiting the clinical utility of RNA hydrogels in malignant tumor diagnostics and therapy. Thus, it is an urgent need to combine RNA hydrogel delivery systems with other therapeutic modalities for developing new therapeutic strategies to overcome the limitations of current therapies for malignant tumors.

Here, an RNA hydrogel-based domino-like cascade reactor RCT-AS1411@Ce6@$SnFe_2O_4$ (designed as RCT-AC@$SnFe_2O_4$) was constructed by incorporating $SnFe_2O_4$ and chlorin e6 (Ce6) into a programmable RNA hydrogel, which integrated quadruple therapeutic modalities such as gene regulation, PDT, CDT and PTT for enhanced anticancer efficacy (Scheme 1). Circular DNA containing microRNA-199a (miR-199a), monocarboxylate transporter 4 small interfering RNA (MCT4 siRNA) and T7 promoter related sequences was used as transcriptional template for amplification reaction. RNA hydrogel (RCT) was transcribed and self-assembled to serve as smart drug delivery carrier to load Ce6-loaded nucleic acid aptamer AS1411@Ce6 (AC) and nanozyme $SnFe_2O_4$. The reactor targeted tumor cells via AS1411 aptamer, degraded hydrogels via intracellular nucleases to release nanozymes, photosensitizers, MCT4 siRNA and miR-199a gene fragments. The photothermal effect of the $SnFe_2O_4$ could be used for PTT, while the increased temperature promoted the disassembly of RNA hydrogel. MCT4 siRNA induced tumor cell acidification by silencing MCT4 and activated mitochondrial biosynthesis by upregulating peroxisome proliferator-activated receptor γ coactivator-1α (PGC1α) in mitochondria, which led to increased H_2O_2 production [38,39]. The $SnFe_2O_4$ nanozyme leveraged its dual enzymatic activities of catalase (CAT) and peroxidase (POD) to efficiently catalyze the conversion of endogenous H_2O_2, driving in situ generation of •OH while simultaneously depleting intracellular GSH, a critical antioxidant reservoir. This cascade reaction consequently compromised the antioxidant defense system of tumor and significantly augmented the CDT efficacy through redox homeostasis disruption. The study indicated that miR-199a directly targeted the 3′-untranslated region (UTR) of hypoxia-inducible factor-1α (HIF-1α), inhibiting tumor cell proliferation by suppressing the HIF-1α/vascular endothelial growth factor (VEGF) signaling pathway [40]. The increase of O_2 during CDT and the inhibition of HIF-1α mediated by miR-199a together promoted Ce6-mediated PDT. This cascade reactor created a synergistic effect among gene regulation, PTT, CDT and PDT, which not only solved the key barrier of current TME targeted therapy but also used programmable nucleic acid hydrogel to coordinate the "gene-PDT-CDT-PTT" interaction, breaking through the limitations of a single treatment model and providing the ideas for the next generation of biocompatibility diagnosis and treatment platform.

2. Experimental section

2.1. Materials

T4 DNA ligase, rNTPs mixture and T7 RNA polymerase were purchased from New England Biolabs. Ce6 was obtained from Shanghai Yuanye Biotechnology Co. Ltd. Tin (II) chloride dihydrate ($SnCl_2{\cdot}2H_2O$), ferrous chloride (II) tetrahydrate ($FeCl_2{\cdot}4H_2O$), ethylene glycol, and 5,5′-dithiobis (2-nitrobenzoic acid) were purchased from Shanghai McLean Bio-Technology Co. Ltd. Cck-8 Cell Proliferation Kit was purchased from Gene-protein link Biotechnology Co., Ltd. Hoechst 33342 was obtained from Thermo Fisher Scientific. Distilled water was used in the experiments after autoclaving. KCl, $MgCl_2$ and other chemicals were analytical reagent grades.

2.2. Preparation of AC

AS1411 apt-Chol and 28 mM Tris-HCl buffer (pH 7.4 containing K^+, Mg^{2+}) were annealed at 95 °C and then slowly colded to room temperature (RT). After Ce6 was added, the reaction was carried out at 25 °C for 2 h. The mixture was finally ultrafiltrated by ultrafiltration tubes to obtained the product AC, which was placed in a standby at 4 °C.

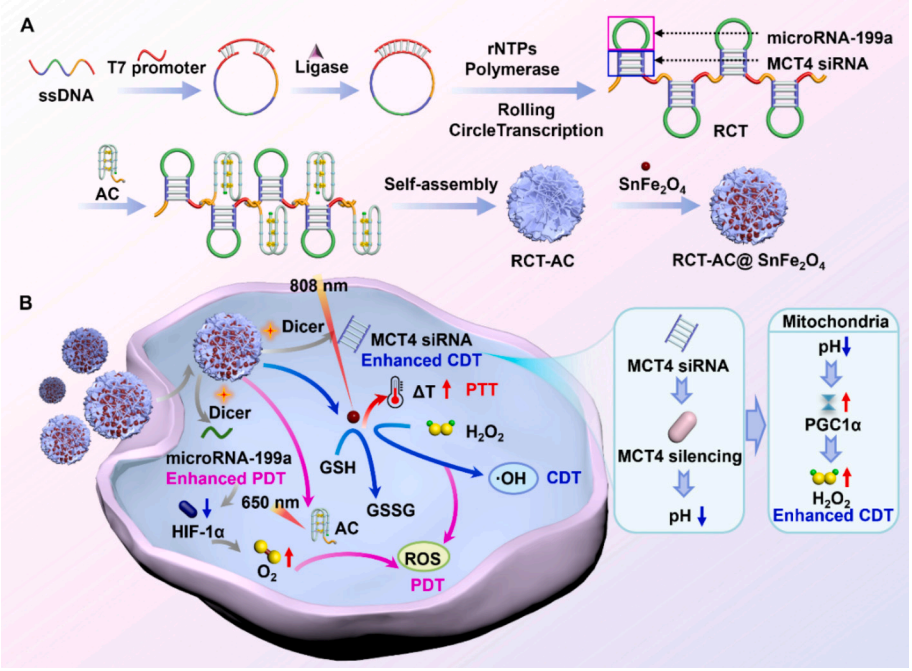

Scheme 1. (A) Synthetic route of RCT-AC@$SnFe_2O_4$. (B) Schematic illustration of RCT-AC@$SnFe_2O_4$ for gene-promoted synergistic cancer therapy.

2.3. Preparation of RCT-AC@$SnFe_2O_4$

RCT and AC were mixed, heated at 95 °C for 5 min, and slowly cooled down to 25 °C to obtain RCT-AC. After RCT-AC was mixed with $SnFe_2O_4$ and shaken at 37 °C for 90 min, the product RCT-AC@$SnFe_2O_4$ was washed by centrifugation (6000 rpm, 10 min).

2.4. Catalytic activity of RCT-AC@$SnFe_2O_4$

To evaluate the peroxidase activity of RCT-AC@$SnFe_2O_4$, the samples were reacted with 5 % H_2O_2, and the O_2 generation was monitored every minute for 30 min. In order to study the consumption of GSH, the sample was reacted with GSH (1 mM) and DTNB (10 mg/mL) at 37 °C for 8 h, centrifuged at 8000 rpm, and the supernatant was retained to detect the UV–vis spectrum. Finally, the ROS generation capacity of RCT-AC@$SnFe_2O_4$ was evaluated. After the samples were mixed with 10 μL of DBPF, the extracellular $^1O_2$ generation capacity was detected by UV–vis spectroscopy. Meanwhile, MCF cells were cultured with RCT-AC@$SnFe_2O_4$, then washed with PBS to incubate with DCFH-DA and Hochest 33,342 for 25 min. The ROS generation of the samples was observed by confocal laser scanning microscope (CLSM).

2.5. Cellular uptake behavior of RCT-AC@$SnFe_2O_4$

RCT-AC@$SnFe_2O_4$ was synthesized using nucleic acid chains labeled with FAM fluorescence. After 1×10^5 cells were co-incubated with therapeutic drugs, the cell nuclei were stained with Hochest 33,342, and finally CLSM and flow cytometry were used to observe the uptake of RCT-AC@$SnFe_2O_4$ by different cells.

2.6. Therapeutic effects of RCT-AC@$SnFe_2O_4$ in vitro

Firstly, cytotoxicity was assessed using the CCK-8 assay. After cells were seeded into a 96-well plate, followed by co-incubation with the drug, CCK-8 solution was added to incubate for 1 h. The absorbance at 450 nm was obtained through a microplate reader. Next, cell apoptosis was detected using a dual fluorescent labeling apoptosis kit. After cells were co-incubated with the therapeutic drugs in a 6-well plate, labeled with the fluorescent markers, they were analyzed using flow cytometry. Meanwhile, the co-incubated cells were stained with trypan blue, and the cell status was observed under a bright-field microscope.

2.7. Therapeutic effect of RCT-AC@$SnFe_2O_4$ in vivo

All animals were obtained from Beijing Vital River Laboratory Animal Technology Co., Ltd. In vivo experiments were performed according to the guidelines of the Institutional Animal Care and Use Committee (2024010A012) approved by Linyi University. After one week of adaptive feeding, all female mice were given estrogen injections, and 10 mg/kg of estradiol benzoate was intraperitoneally injected twice a week for 2 weeks. 100 μL of MCF-7 cell suspension was subcutaneously injected into mice, and 10 mg/kg of estradiol formate was intraperitoneally injected every other day after inoculation. After 10 days, the successfully inoculated mice were divided into groups at random and treated as follows: Ce6 + 650 nm, RCT-AC + 650 nm, $SnFe_2O_4$ + 808 nm, RCT@$SnFe_2O_4$ + 808 nm, PBS RCT-AC@$SnFe_2O_4$, and RCT-AC@$SnFe_2O_4$ + 650 nm + 808 nm. The status of the mice was continuously tracked, and the solid tumor volume and body weight of the mice were recorded. The mice were killed using CO_2 after treatment. The tumors and major organs of the mice were dissected and separated and fixed with tissue fixative. The fixed tissue structure was dehydrated, embedded, and then sectioned. The samples prepared were stained with hematoxylin-eosin (H&E) dyes and observed and photographed under a bright field microscope.

2.8. Statistical analysis

The data were presented as the means ± standard deviations (SD) from in vitro and in vivo measurements, which were also statistically analyzed using Student's *t*-test. $^*p < 0.05$, $^{**}p < 0.01$, $^{***}p < 0.001$ and $^{****}p < 0.0001$ were statistically significant and extremely significant, respectively.

3. Results and discussion

3.1. Synthesis and characterization of RCT-AC@$SnFe_2O_4$

This study engineered a circular DNA template capable of transcribing sequences encoding miR-199a and MCT4 siRNA to generate RNA hydrogel (RCT), with detailed nucleic acid sequences provided in Table S1. The AS1411 sequence, enriched in guanine (G), was self-assembled into G-quadruplex structure in the presence of K^+, enabling the encapsulation of the photosensitizer Ce6 to form the AC. This AC product was subsequently hybridized with RCT via Watson-Crick base pairing, yielding the RCT-AC composite. Finally, $SnFe_2O_4$ was loaded onto RCT-AC through electrostatic interaction, culminating in the fabrication of the cascaded therapeutic reactor, designated as RCT-AC@$SnFe_2O_4$. The RCT-AC@$SnFe_2O_4$ nanocomplex achieved tumor-targeted cellular internalization through AS1411 aptamer-mediated recognition. Following cellular internalization, endogenous dicer enzymes selectively cleaved the hydrogel scaffold, while the photothermal conversion capability of $SnFe_2O_4$ under 808 nm laser irradiation further accelerated hydrogel degradation, thereby triggering the release of therapeutic gene fragments and encapsulated drugs.

AC and $SnFe_2O_4$ were synthesized following established procedures (Scheme 1A) [41,42]. The amount of Ce6 loaded onto the synthesized AC was optimized with fluorescence and UV–vis spectrometric measurements (Figs. S1 and S2). As the proportion of Ce6 increased, the fluorescence intensity and UV–vis absorption gradually increased, and the optimal ratio of AS1411 to Ce6 was 1:8, which ensured an ample supply of photosensitizer essential for PDT achievement. Subsequently, transmission electron microscopy (TEM) was used to visualize the internal structure and diameter of $SnFe_2O_4$, RCT and RCT-AC, respectively (Fig. 1A-1C). The formation of nanoflowers with a porous structure of RCT is facilitated by the generation of pyrophosphate anions (PPi^{4-}) throughout the transcription process. The addition of cholesterol to the end of AS1411 gave the hydrogel spatial confinement. Due to the hydrophobic effect of cholesterol, the size of RCT-AC was significantly reduced. In addition, cholesterol improved in vivo transfection efficiency and protected miRNA/siRNA from degradation. The scanning electron micrography-energy dispersive X-ray spectroscopic (SEM-EDS) mapping analysis showed the key elements C, O and N, DNA characteristic element P, and the presence of Fe and Sn (Fig. 1D), demonstrating the elemental spatial distribution characteristics of the domino-like cascade reactor RCT-AC@$SnFe_2O_4$. Part of the Mg signal was derived from magnesium pyrophosphate (Mg_2PPi) formed during the preparation of RCT nanoflowers. The results preliminarily confirmed the successful synthesis of RCT-AC@$SnFe_2O_4$. Agarose gel electrophoresis was employed to characterize the transcription product, revealing distinct electrophoretic mobility of the RNA hydrogel corresponding to the varying molecular weight (Fig. S3). Due to the large number of transcript copies produced by rolling circle transcription, RCT and RCT-AC showed larger molecular weights than the template and/or primer, leading to slower migration. The results confirmed the successful synthesis of RCT and RCT-AC.

The incorporation of AC was verified with fluorescence and UV–vis spectroscopic analyses. The stronger fluorescence and absorption intensity of RCT-AC than RCT indicated that AC was successfully loaded onto RCT (Fig. 1E and F). The Zeta potentials showed the negatively charged surface of RCT-AC@$SnFe_2O_4$, which was weaker than that of RCT-AC due to the positive charge on the surface of the $SnFe_2O_4$. The

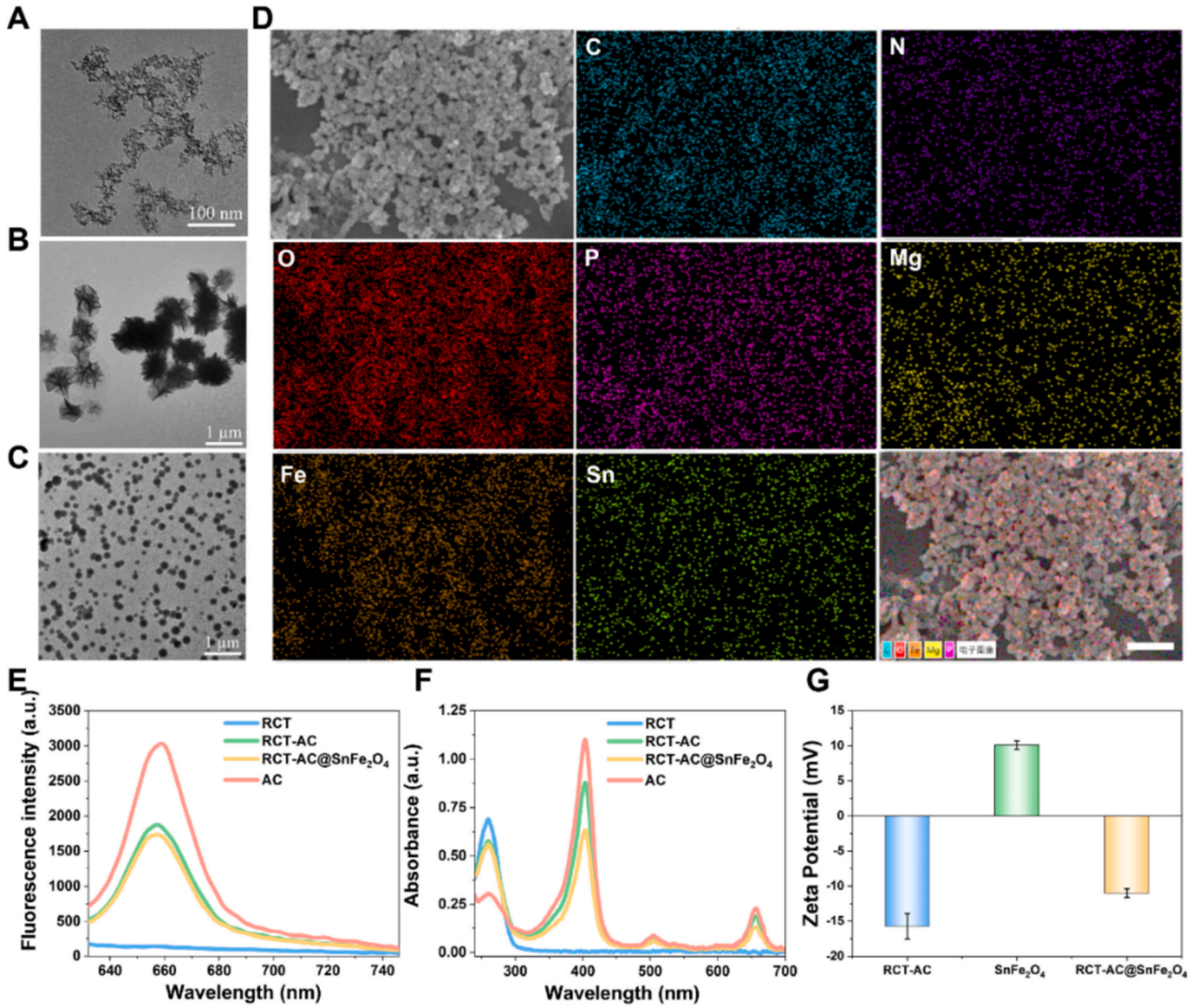

Fig. 1. (A) TEM images of $SnFe_2O_4$, (B) RCT and (C) RCT-AC. (D) SEM images and SEM-EDS mapping of RCT-AC@$SnFe_2O_4$. Scale bar, 1 μm. (E) Fluorescence spectra and (F) UV–vis spectra of AC, RCT, RCT-AC and RCT-AC@$SnFe_2O_4$. (G) Zeta potentials of $SnFe_2O_4$, RCT-AC, and RCT-AC@$SnFe_2O_4$. $n = 3$.

positive electrical properties of $SnFe_2O_4$ promoted its binding with RNA hydrogel through electrostatic interaction. The results proved the successful loading of $SnFe_2O_4$ on RCT-AC (Fig. 1G), demonstrating the successful synthesis of domino-like cascade reactor RCT-AC@$SnFe_2O_4$.

3.2. *Properties of RCT-AC@$SnFe_2O_4$*

Firstly, the catalase catalytic properties of RCT-AC@$SnFe_2O_4$ were validated by assessing its ability to catalyze the generation of O_2 from H_2O_2, utilizing a dissolved oxygen meter (Fig. 2A). Upon the addition of the nanozyme, the O_2 concentration in the solution increased continuously. Incorporating the nanozymes into RNA hydrogel did not impair the catalytic activity of $SnFe_2O_4$ with respect to the disproportionation of hydrogen peroxide. The results demonstrated that RCT-AC@$SnFe_2O_4$ had peroxidase catalytic properties. In addition, 5,5′-dithiobis-(2-nitrobenzoic acid) (DTNB) was employed as an indicator for the detection of GSH consumption (Fig. 2B). After DTNB reacted with the sulfhydryl group (-SH) in GSH, which showed the maximum UV–vis absorption peak at 412 nm, yellow 5-thiobenzoic acid was produced. The addition of nanozyme decreased significantly the UV–vis absorption at 412 nm, indicating the obvious promotion of nanozyme to the consumption of GSH due to the relatively high level of ROS.

The generation of singlet oxygen ($^1O_2$) in vitro was detected using 1,3-diphenylisobenzofuran (DPBF) as an indicator (Fig. 2C). The double laser-irradiated RCT-AC@$SnFe_2O_4$ produced a large amount of $^1O_2$ outside the cells, causing dramatic decrease of the absorbance of DPBF. The fluorescence staining assay verified that RCT-AC@$SnFe_2O_4$ could effectively generate ROS in living cells (Fig. 2D). In addition to the cytotoxic $^1O_2$ generated by photodynamic therapy, H_2O_2 could activate CDT to produce in situ ·OH through Fenton-like reaction, which was detected using 2′,7′-dichlorodihydrofluorescein diacetate (DCFH-DA). DCFH-DA is non-fluorescent and can freely traverse the cell membrane. After transfecting DCFH-DA into the cells, the intensity of intracellular green fluorescence (2′,7′-dichlorofluorescein, DCF) is directly proportional to the ROS levels [43]. Consistent with the results of the extracellular assay, the DCF fluorescence intensity increased dramatically after the cells were treated with RCT-AC@$SnFe_2O_4$ and dual-wavelength irradiation. However, in the absence of RCT-AC@$SnFe_2O_4$, DCF fluorescence remained constant at low levels. These results indicated that RCT-AC@$SnFe_2O_4$ could effectively generate multiple types of ROS

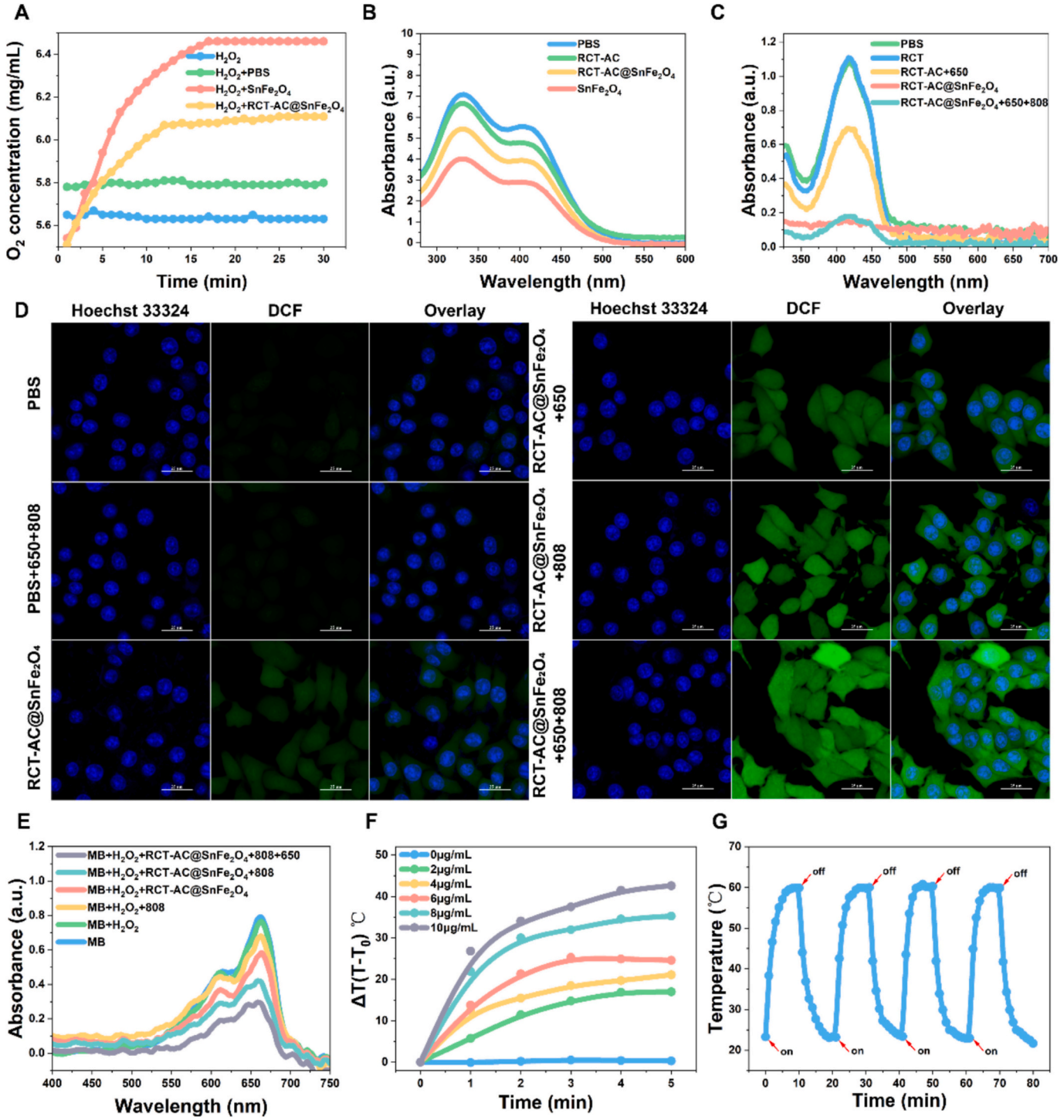

Fig. 2. (A) Oxygen content of different samples. (B, C) UV–Vis spectra of different samples after reacted with DTNB (B) and DPBF (C). (D) CLSM images of MCF-7 cells treated under different conditions. (E) UV–vis spectra of MB solutions after different treatments. (F) Temperature change curves of RCT-AC@$SnFe_2O_4$ at different concentrations. (G) Thermal stability of RCT-AC@$SnFe_2O_4$.

including $^1O_2$.

In addition, methylene blue (MB) was used as an indicator to evaluate the ability of RCT-AC@$SnFe_2O_4$ to produce ·OH. The absorbance of MB was significantly reduced MB was incubated with RCT-AC@$SnFe_2O_4$ and H_2O_2, while the absorbance of MB did not significantly change after it was treated with H_2O_2 alone (Fig. 2E). Meanwhile, with the increasing RCT-AC@$SnFe_2O_4$ concentration and the decreasing solution pH, the production of ·OH gradually increased (Fig. S4). These results indicated that RCT-AC@$SnFe_2O_4$ could induce Fenton-like reaction in the tumor microenvironment to effectively produced ·OH through following reactions, revealing the possibility of RCT-AC@$SnFe_2O_4$ for CDT.

$$Fe^{2+}/Sn^{2+} + H_2O_2 \rightarrow \cdot OH + Fe^{3+}/Sn^{4+}$$

$$Fe^{3+}/Sn^{4+} + H_2O \rightarrow Fe^{2+}/Sn^{2+} + O_2$$

$$O_2 \xrightarrow{Ce6} {}^1O_2$$

$$Fe^{3+}/Sn^{4+} + GSH \rightarrow Fe^{2+}/Sn^{2+} + GSSG$$

The photothermal properties of RCT-AC@$SnFe_2O_4$ were subsequently examined. After the samples were irradiated with an 808 nm laser at a power density of 1 W/cm^2 for increasing time, the temperature of RCT-AC@$SnFe_2O_4$ gradually increased and showed obvious concentration dependences. Specifically, when the concentration was 10 μg/mL, the temperature rapidly increased by nearly 30 °C, while the temperature change of the blank control group was almost negligible (Figs. 2F and S5). Upon exposure to 808-nm laser, the maximum temperature difference reached 40 °C within 10 min, and the temperature returned to baseline within 10 min after ceasing laser exposure (Fig. S6). From the linear plot of the time point of the cooling phase vs -ln(θ) (R^2 = 0.992) (Fig. S7), the conversion efficiency (η) of RCT-AC@$SnFe_2O_4$ was calculated to be 23.62 % at 808 nm, which was slightly higher than 22 % of gold nanorods [44]. Additionally, heating and cooling cycle curves demonstrated the photothermal stability of RCT-AC@$SnFe_2O_4$, with negligible change in photothermal conversion performance after multiple cycles (Fig. 2G). These results demonstrated that RCT-AC@$SnFe_2O_4$ possessed good photothermal performance and exceptional thermal stability.

3.3. Uptake and synergistic therapeutic effect of RCT-AC@$SnFe_2O_4$ in vitro

To confirm the tumor cell-targeting capability of the RCT-AC@$SnFe_2O_4$, its uptake by tumor cells was assessed using L02 cell line as a control. The presence of AS1411 in RCT-AC@$SnFe_2O_4$ imparted specific recognition ability for nucleolin. After MCF-7 and L02 cells were cultured with RCT-AC@$SnFe_2O_4$ for 2 h, and their nuclei were stained with Hochest 33,342, MCF-7 cells showed stronger fluorescence than L02 cells. The results indicated that RCT-AC@$SnFe_2O_4$ could target to tumor cells through aptamer (Fig. 3A). Flow cytometric data confirmed this phenomenon (Fig. 3B). Moreover, confocal laser imaging and flow cytometry showed gradually increased fluorescence intensity in tumor cells, indicating that RCT-AC@$SnFe_2O_4$ effectively accumulated in tumor cells (Figs. S8 and S9). These results illustrated that RCT-AC@$SnFe_2O_4$ could accurately target tumor cells to reduce toxic and

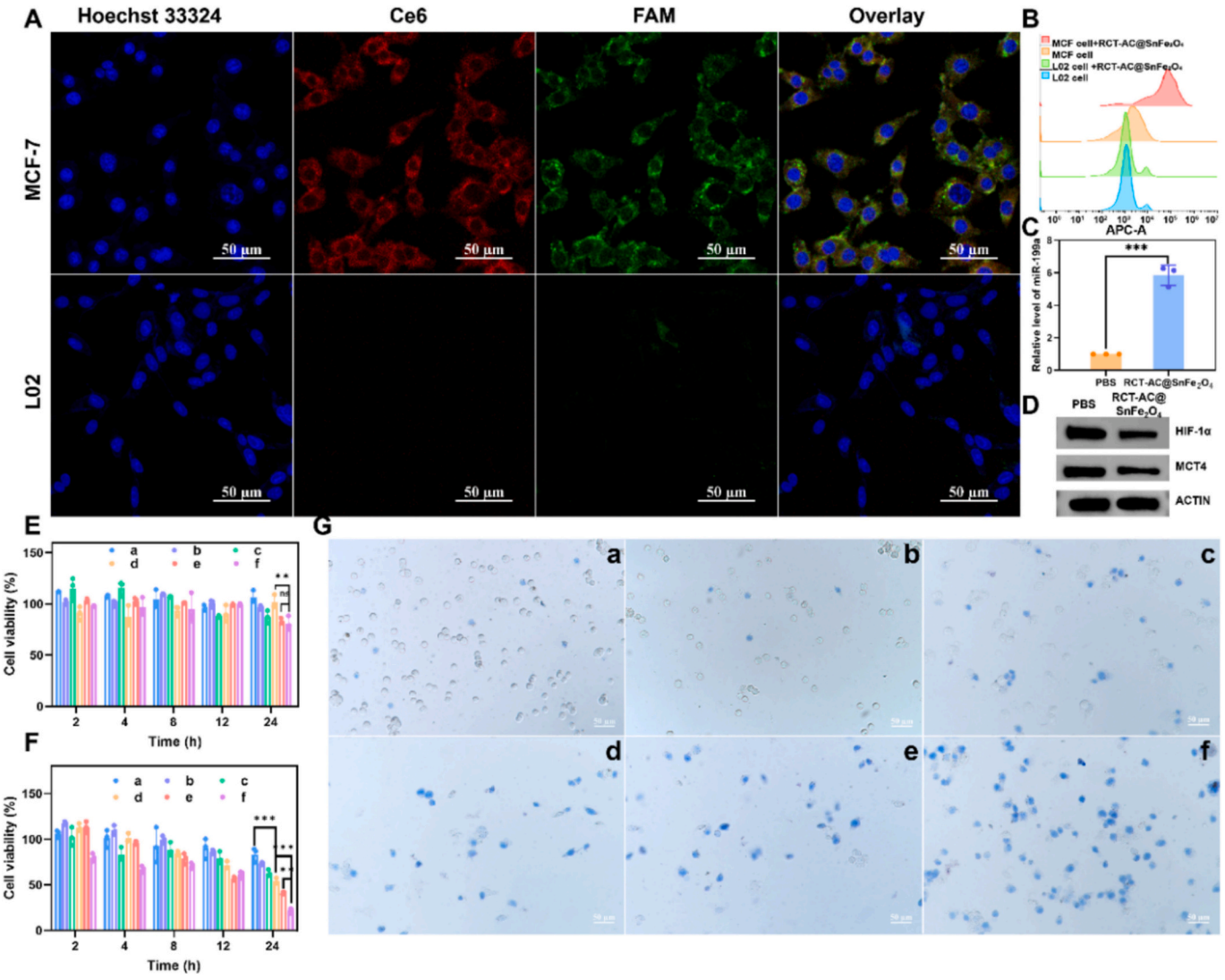

Fig. 3. (A) CLSM images of MCF-7 and L02 cells after RCT-AC@$SnFe_2O_4$ treatment. Scale bar: 50 μm. (B) Flow cytometric analysis of MCF-7 and L02 cells incubated with RCT-AC@$SnFe_2O_4$. (C) Expression of miR-199a in MCF-7 cells incubated with PBS and RCT-AC@$SnFe_2O_4$. $n = 3$. Student's t-test, $^{***}p < 0.001$. (D) Western blot detection of protein expression using ACTIN as a loading control. Cytotoxicity of different treatments on L02 (E) and MCF-7 (F) cells. $n = 3$. Student's t-test, ns: not significant, $^{*}p < 0.05$, $^{**}p < 0.01$, $^{***}p < 0.001$. (G) Bright-field microscopic images of MCF-7 cells after different treatments and stained with trypan blue. Scale bar: 50 μm. a: Ce6 + 650 nm, b: RCT-AC + 650 nm, c: $SnFe_2O_4$ + 808 nm, d: RCT@$SnFe_2O_4$ + 808 nm, e: RCT-AC@$SnFe_2O_4$, and f: RCT-AC@$SnFe_2O_4$ + 650 nm + 808 nm.

side effects on normal cells.

Polyacrylamide gel electrophoresis (PAGE) analysis was performed to verify the release of gene fragments in cells (Fig. S10), which showed small nucleic acid products upon the addition of RNaseIII, highly consistent with the cleavage characteristics of Dicer enzyme in cells. It is worth noting that this result validated the controlled release of gene fragments in the intracellular environment, providing an important experimental basis for subsequent enhancement of tumor therapeutic effects. To examine the release of miRNA in cells, the expression of miR-199a in cells was verified by qPCR assay. The primer sequences used in the qPCR experiments were detailed in Table S2. The expression level of specific miRNA-199a in tumor cells was significantly up-regulated after treatment with RCT-AC@$SnFe_2O_4$ (Fig. 3C). As a negative regulator of HIF-1α, miRNA-199a effectively inhibited the synthesis of HIF-1α protein. Western blot analysis demonstrated a significant down-regulation of HIF-1α and MCT4 expression in tumor cells following RCT-AC@$SnFe_2O_4$ treatment (Fig. 3D). The reduction in HIF-1α level suggested that the treatment effectively alleviated hypoxia within the TME. Furthermore, the decreased MCT4 expression indicated impaired lactate efflux capacity in tumor cells, which might alter intracellular pH homeostasis and consequently suppress their invasive and metastatic potential. Meanwhile, the changes of H_2O_2 levels were examined after cell lysis from different treatment groups. The intracellular H_2O_2 contents in different groups were significantly higher than that in PBS group, and the double laser irradiation cascade reactor treatment group showed the most significant increase (Fig. S11). The increase in H_2O_2 level provided a key prerequisite for subsequent ROS-based synergistic therapy. On the one hand, the elevated H_2O_2 could be used as enough substrate for CDT to generate highly cytotoxic ·OH through Fenton reaction. On the other hand, the gradient distribution of H_2O_2 also confirmed the differential regulation ability of different treatment strategies on the tumor oxidative stress microenvironment, which provided a molecular basis for optimizing the combined treatment strategy. The changes in gene, protein and compound levels provided important references for the subsequent optimization of synergistic treatment strategies.

Next, the cytotoxicity of RCT-AC@$SnFe_2O_4$ was evaluated using CCK-8 cell proliferation-toxicity detection kit. MCF-7 under hypoxic conditions and L02 cells were incubated with different treatment groups. Upon the incubation L02 cells showed negligible difference (Fig. 3E). Compared to Ce6 + 650 nm treatment group, the therapeutic efficacy of RCT-AC + 650 nm on MCF-7 cells was enhanced, indicating that the miR-199a sequence in RNA hydrogel facilitated Ce6-mediated PDT. Additionally, $SnFe_2O_4$ + 808 nm treatment group exhibited superior therapeutic effect relative to RCT-AC + 650 nm group, which could be attributed to the combined weak photodynamic effect, the production of ·OH via chemical kinetics, and the efficient photothermal effect of $SnFe_2O_4$ + 808 nm treatment. Furthermore, compared to $SnFe_2O_4$ + 808 nm treatment group, RCT@$SnFe_2O_4$ + 808 nm group showed enhanced therapeutic efficacy, suggesting that the MCT4 siRNA sequence in the hydrogel promoted $SnFe_2O_4$-mediated CDT. It was worth noting that RCT-AC@$SnFe_2O_4$ treatment group irradiated with dual lasers had a significant inhibitory effect on the proliferation of MCF-7 cells compared with other control groups (Fig. 3F). Meanwhile, the accumulation of drugs in MCF-7 cells made the inhibition to their growth more significant.

The apoptosis of MCF-7 cells was analyzed using double staining with Annexin V-FITC and PI. First, forward scatter height (FSC-H) -forward scatter area (FSC-A) was used to exclude cell aggregation and select singlet states. Then the cells were initially gated on FSC/SSC to exclude debris. Next, quadrants were established using unstained and single-stained controls. Annexin V^-/PI^+, Annexin V^+/PI^+, Annexin V^+/PI^-, and Annexin V^-/PI^- respectively represent necrotic, late apoptotic, early apoptotic, and viable cells. Finally, fluorescence compensation was adjusted by a single staining control to eliminate spectral overlap. The total apoptosis rate was calculated as the sum of late and early apoptotic cells. The results were consistent with those observed from in vitro cytotoxicity measurements, demonstrating that the RCT-AC@$SnFe_2O_4$ + 650 nm + 808 nm treatment group exhibited remarkable advantages compared with other control groups (Fig. S12). To further elaborate the therapeutic effects of different treatment groups on MCF-7 cells, trypan blue was used as a cell viability dye for the assessment of cell membrane integrity and MCF-7 cell viability [45]. RCT- AC@$SnFe_2O_4$ + 650 nm + 808 nm treatment group showed more number of cells stained in blue than other treatment groups (Fig. 3G), confirming the potential advantages of dual-laser irradiated domino-like cascade reactor RCT-AC@$SnFe_2O_4$ in cancer therapy.

Compared with the traditional inorganic cascade strategies, such as Cu_2MoS_4-based multifunctional bioreactor [46], the cascade reactor showed unique advantages. The programmability of nucleic acid sequence endowed the carrier the ability to target specific signal responses in TME, which achieved accurate release of drug/enzyme in the lesion site, and thus significantly improving the treatment specificity and reducing side effects. The hydrogel network could be loaded with photosensitizers and nanozymes with high efficiency. The nucleic acid backbone itself could also be used as a carrier for therapeutic nucleic acids, which was expected to further achieve more flexible and powerful functional integration of diagnosis and treatment.

3.4. *Uptake and synergistic therapeutic effect of RCT-AC@$SnFe_2O_4$ in vivo*

The therapeutic properties of the cascade reactor RCT-AC@$SnFe_2O_4$ were further examined using a mouse model with subcutaneous MCF-7 breast cancer tissue. Each group of mice was given different treatment drugs, maintaining a consistent injection dose and injection frequency (Fig. 4A). Inspired by the in vitro studies, the accumulation and retention capacity of RCT-AC@$SnFe_2O_4$ at tumor location were examined, which showed a continuous enhancement of RCT-AC@$SnFe_2O_4$ fluorescence within 0.5 h after tail vein injection, and reached the maximum at 8 h (Fig. 4B). The semiquantitative analysis of fluorescence images at the tumor site showed clear fluorescence signals at 0.5 h, which reached the maximum at 8 h after RCT-AC@$SnFe_2O_4$ injection (Fig. 4C). In addition, fluorescence imaging was performed on major organs and tumor tissues of mice at 48 h after tail vein injection (Fig. 4D). The semiquantitative analysis showed that RCT-AC@$SnFe_2O_4$ had excellent tumor targeting and enhanced retention (Fig. 4E). The excellent tumor accumulation ability should be attributed to the targeting ability of aptamer AS1411. The tumor size and body weight of each mouse were monitored during the treatment (Figs. 4F and S13). Tumor growth was observed to be inhibited to varying extents. Significantly, due to the positive effects of various components in the cascade reactor, the synergistic effect of the RCT-AC@$SnFe_2O_4$ resulted in substantial tumor suppression within 14 days. The exceptional anticancer efficacy of the RCT-AC@$SnFe_2O_4$ was further validated by the tumor weight post-treatment (Fig. S14) and visual evidence from images of the tumors and mice (Figs. 4G and S15).

Histopathological evaluation of tissues and organs were performed after systematically therapeutic to assess treatment-induced histopathological alterations. H&E staining analysis demonstrated that severe tissue destruction occurred in the treatment group of the double laser irradiated cascade reactor RCT-AC@$SnFe_2O_4$ compared with PBS group (Fig. 4H). TUNEL assay was performed separately on the tumors of each group of mice (Fig. 4I). The apoptotic tumor tissue cells showed green fluorescence, and the normal tumor tissue cells showed blue fluorescence. RCT- AC@$SnFe_2O_4$ + 650 nm + 808 nm resulted in the highest level of apoptosis. Semi-quantitative analysis indicated that the double laser irradiated cascade reactor RCT-AC@$SnFe_2O_4$ significantly promoted tumor apoptosis, which was consistent with in vitro results (Fig. S16). The change of Ki67 expression level after tumor treatment was an important indicator to evaluate the efficacy and prognosis. To further validate the treatment effect, immunohistochemical analysis of Ki67 was performed to assess the tumor cell proliferation. The results

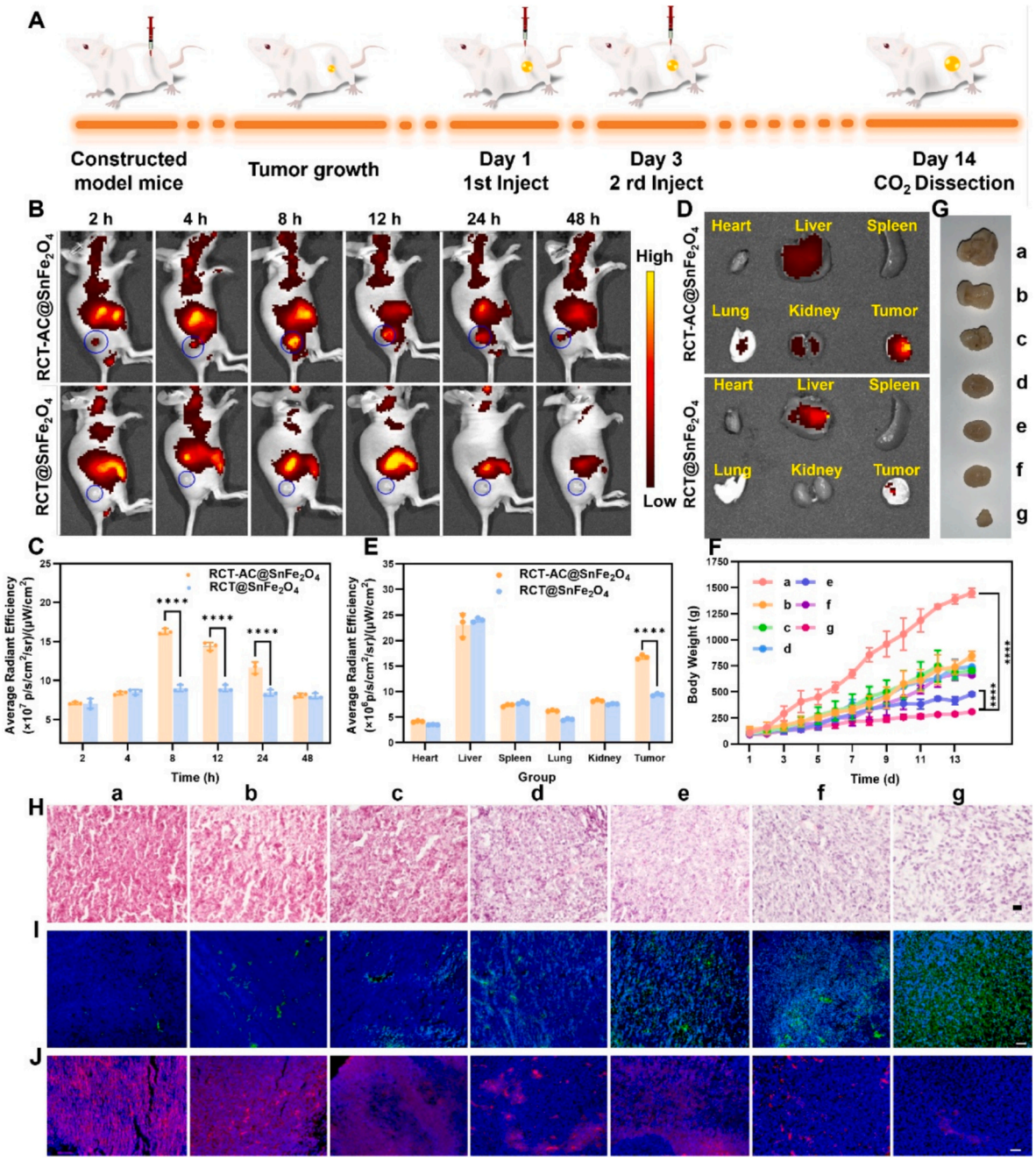

Fig. 4. (A) Schematic diagram of in vivo study of RCT-AC@$SnFe_2O_4$. (B) Fluorescence images of MCF-7 hormonal mice were observed after intravenous injection of RCT-AC@$SnFe_2O_4$. (C) Relative tumor fluorescence intensity based on in vivo fluorescence images in (B), $n = 3$. Student's *t*-test, $^{****}p < 0.0001$. (D) Fluorescence images of tumors and organs at the end of the study (48 h after injection) and semiquantitative analysis (E), $n = 3$. Student's *t*-test, $^{****}p < 0.0001$. (F) Tumor volume changes over 14 days after different treatments. Tumor volume: width^2 × length/2, $n = 3$. Student's *t*-test, $^{****}p < 0.0001$. (G) Representative photos of the mice after various treatments. (H) H&E staining of tumor. Scale bar: 20 μm. (I) TUNEL and (J) Ki67 immunofluorescence staining of tumor tissues excised by different treatments. Scale bar: 50 μm. a: PBS, b: Ce6 + 650 nm, c: RCT-AC + 650 nm, d: $SnFe_2O_4$ + 808 nm, e: RCT@$SnFe_2O_4$ + 808 nm, f: RCT-AC@$SnFe_2O_4$, and g: RCT-AC@$SnFe_2O_4$ + 650 nm + 808 nm.

showed the inhibited expression of Ki67 in tumors after treatment with different drugs (Fig. 4J). Semiquantitative analysis showed significantly reduced expression level of Ki67 in tumor tissues after treatment with the dual laser irradiated cascade reactor RCT-AC@$SnFe_2O_4$ (Fig. S17), suggesting that the reactor synergistically promoted the apoptosis by inhibiting tumor cell proliferation, which might involve DNA damage and cell cycle arrest caused by multiple effects of photothermal, photodynamic and chemical kinetics.

After 14 days of treatment, blood biochemical parameters were measured in PBS group and the dual laser irradiated reactor treated group (Fig. S18). The blood analysis indicated that the routine blood parameters of the two groups were maintained within the normal physiological range. Thus the treatment did not cause obvious hematological toxicity or systemic adverse reactions. Finally, the biosafety of the cascade-reactor was tested by H&E staining of the main tissues and organs (Fig. S19), no pathological abnormality was observed in H&E staining of major organs of mice in all groups, and the body weight of mice remained stable. These findings indicated that the RNA hydrogel-based cascade reactor RCT-AC@$SnFe_2O_4$ possessed good biosafety and could enhance the cancer therapy.

4. Conclusion

In summary, this study constructed a cascade reactor RCT-AC@Sn-Fe_2O_4 by mixing photosensitizer and nanozyme in RNA hydrogel to realize the synergistic treatment for malignant tumors. The interaction between the components in the cascade reactor and TME was utilized to form an intelligent and interconnected reaction network. After systemic administration, intracellular dicer enzyme degraded the hydrogel, while external 808 nm laser irradiation activated the reactor for PTT. The elevated temperature accelerated the release of the drug, MCT4 siRNA and miR-199a gene fragments from the hydrogel carrier. MCT4 siRNA induced cell acidification and further promoted H_2O_2 level in mitochondria by silencing MCT4. The $SnFe_2O_4$ responded to the degradation of H_2O_2 and GSH in cells and produced a large amount of ·OH to achieve gene promotion of CDT. In addition, miR-199a enhanced Ce6-mediated PDT by inhibiting HIF-1α expression and consumption of H_2O_2 of $SnFe_2O_4$ to increase intracellular O_2 level, which resulted in a synergistic effect of gene promotion, CDT and PDT. The designed intelligent domino-like cascade reactor maximized the use of each component of TME, and significantly improved the therapeutic effect of cancer. This study also demonstrated the potential of RNA hydrogels in the diagnosis and treatment of malignant tumors.

CRediT authorship contribution statement

Xiaofan Liu: Writing – original draft, Investigation, Formal analysis, Data curation, Conceptualization. **Yun Yin:** Investigation, Data curation. **Jiajia Zhu:** Investigation, Data curation. **Ziyang Song:** Investigation, Data curation. **Weicai Wang:** Investigation, Data curation. **Xuemei Li:** Writing – review & editing, Supervision, Investigation, Funding acquisition. **Huangxian Ju:** Writing – review & editing, Supervision.

Declaration of competing interest

The authors declare that they have no known competing financial interests or personal relationships that could have appeared to influence the work reported in this paper.

Acknowledgments

This work was supported by the National Natural Science Foundation of China (21876074), Taishan Scholars Project of Shandong Province (No. tsqn201812101).

Appendix A. Supplementary data

Supplementary data to this article can be found online at https://doi.org/10.1016/j.cej.2025.168338.

Data availability

Data will be made available on request.

References

[1] Z. Li, Y. Deng, H. Sun, C. Tan, H. Li, F. Mo, Y. Wang, J. Li, Z. Zhou, M. Sun, Redox modulation with a perfluorocarbon nanoparticle to reverse Treg-mediated immunosuppression and enhance anti-tumor immunity, J. Control. Release 358 (2023) 579–590, https://doi.org/10.1016/j.jconrel.2023.05.013.
[2] J. Wang, L. Li, Z.P. Xu, Enhancing cancer chemo-immunotherapy: innovative approaches for overcoming immunosuppression by functional nanomaterials, Small Methods 8 (2024) 2301005, https://doi.org/10.1002/smtd.202301005.
[3] H. Zhao, Z. Wang, S. Yang, R. Zhang, J. Guo, D. Yang, Energy-storing DNA-based hydrogel remodels tumor microenvironments for laser-free photodynamic immunotherapy, Biomaterials 309 (2024) 122620, https://doi.org/10.1016/j.biomaterials.2024.122620.
[4] Y. Wang, S. Sun, Z. Zhang, D. Shi, Nanomaterials for cancer precision medicine, Adv. Mater. 30 (2018) 1705660, https://doi.org/10.1002/adma.201705660.
[5] X. Fu, Y. Yao, Q. Liu, Z. Guo, C. Yan, W.-H. Zhu, Self-adaptive photodynamic therapy for boosting therapeutic efficiency in tumor, Sci. China Chem. (2025), https://doi.org/10.1007/s11426-024-2559-1.
[6] K. Musaie, S. Abbaszadeh, K. Marais, V. Nosrati-Siahmazgi, S. Rezaei, B. Xiao, K. Dua, H.A. Santos, M. Shahbazi, H_2O_2-generating advanced nanomaterials for cancer treatment, Adv. Funct. Mater. (2025) 2425866, https://doi.org/10.1002/adfm.202425866.
[7] S. Bi, X. Wen, G. Sun, S. Zeng, Activatable NIR-II ratiometric fluorescence nanoprobe for in vivo real-time dynamic imaging of GSH and its-associated diseases, Nano Today 53 (2023) 102027, https://doi.org/10.1016/j.nantod.2023.102027.
[8] J. Zhang, J. Hu, W. Zhu, Y. Liu, S. Li, H. Chen, F. Liao, Q. Zhang, X. Sun, X. Li, Y. Xiao, J. Chen, Hypoxia-triggered tumor specific glutamine inhibition for reversing cisplatin resistance of chemotherapy, Chem. Eng. J. 479 (2024) 147692, https://doi.org/10.1016/j.cej.2023.147692.
[9] Q. Wu, Q. Du, X. Sun, M. Niu, L. Tan, C. Fu, X. Ren, Y. Zheng, T. Liang, J. Zhao, X. Lv, P. Liang, D. Yang, X. Meng, J. Yu, MnMOF-based microwave-glutathione dual-responsive nano-missile for enhanced microwave Thermo-dynamic chemotherapy of drug-resistant tumors, Chem. Eng. J. 439 (2022) 135582, https://doi.org/10.1016/j.cej.2022.135582.
[10] M. Ding, W. Liu, R. Gref, Nanoscale MOFs: from synthesis to drug delivery and theranostics applications, Adv. Drug Deliv. Rev. 190 (2022) 114496, https://doi.org/10.1016/j.addr.2022.114496.
[11] Z.-A. Chen, C.-H. Wu, S.-H. Wu, C.-Y. Huang, C.-Y. Mou, K.-C. Wei, Y. Yen, I.-T. Chien, S. Runa, Y.-P. Chen, P. Chen, Receptor ligand-free mesoporous silica nanoparticles: a streamlined strategy for targeted drug delivery across the blood–brain barrier, ACS Nano 18 (2024) 12716–12736, https://doi.org/10.1021/acsnano.3c08993.
[12] J. Tang, A.K. Meka, S. Theivendran, Y. Wang, Y. Yang, H. Song, J. Fu, W. Ban, Z. Gu, C. Lei, S. Li, C. Yu, Openwork@dendritic mesoporous silica nanoparticles for lactate depletion and tumor microenvironment regulation, Angew. Chem. Int. Ed. 59 (2020) 22054–22062, https://doi.org/10.1002/anie.202001469.
[13] W. Wang, Y. Yang, X. Chen, T. Zhao, X. Li, Hollow mesoporous MnO_2 nanospheres as light source-free carriers for synergistic starvation and chemiexcited photodynamic tumor therapy, ACS Appl. Nano Mater. 6 (2023) 15314–15323, https://doi.org/10.1021/acsanm.3c03336.
[14] J. Liu, L. Miao, J. Sui, Y. Hao, G. Huang, Nanoparticle cancer vaccines: design considerations and recent advances, Asian J. Pharm. Sci. 15 (2020) 576–590, https://doi.org/10.1016/j.ajps.2019.10.006.
[15] G. Ke, M. Liu, S. Jiang, X. Qi, Y.R. Yang, S. Wootten, F. Zhang, Z. Zhu, Y. Liu, C. J. Yang, H. Yan, Directional regulation of enzyme pathways through the control of substrate channeling on a DNA origami scaffold, Angew. Chem. Int. Ed. 55 (2016) 7483–7486, https://doi.org/10.1002/anie.201603183.
[16] M. Moazzam, M. Zhang, A. Hussain, X. Yu, J. Huang, Y. Huang, The landscape of nanoparticle-based siRNA delivery and therapeutic development, Mol. Ther. 32 (2024) 284–312, https://doi.org/10.1016/j.ymthe.2024.01.005.
[17] S. Li, X. Zhu, H. Liu, B. Sun, Recent advances of covalent organic framework-based nanozymes for energy conversion, Coord. Chem. Rev. 518 (2024) 216046, https://doi.org/10.1016/j.ccr.2024.216046.
[18] S. Sarkar, D. Malhotra, M. Debnath, G.C. Kundu, R. Srivastava, A.R. Kulkarni, Rationalizing defective biomimetic ceria: in vitro demonstration of a potential "trojan horse" nanozyme based-platform leveraging photo-redox activities for minimally invasive therapy, Adv. Mater. Technol. 10 (2025) 2400556, https://doi.org/10.1002/admt.202400556.
[19] Q. Tian, H. Wang, S. Huangfu, R. Yang, Y. Chen, J. Gao, Y. Yang, L. Zhang, Oxygen vacancy formation energy determines the phase-activity relationship of MnO_2 laccase nanozymes, ACS Appl. Mater. Interfaces (2025) acsami.4c22599, https://doi.org/10.1021/acsami.4c22599.
[20] W. Gong, A multichannel nucleic acid-based Ca^{2+} nanomodulator induces multilevel destruction of mitochondria for cancer therapy, Nano Today 58 (2024) 102465, https://doi.org/10.1016/j.nantod.2024.102465.
[21] Y. Zhang, L. Zhu, J. Tian, L. Zhu, X. Ma, X. He, K. Huang, F. Ren, W. Xu, Smart and functionalized development of nucleic acid-based hydrogels: assembly strategies, recent advances, and challenges, Adv. Sci. 8 (2021) 2100216, https://doi.org/10.1002/advs.202100216.
[22] N. Oliva, J. Conde, K. Wang, N. Artzi, Designing hydrogels for on-demand therapy, Acc. Chem. Res. 50 (2017) 669–679, https://doi.org/10.1021/acs.accounts.6b00536.
[23] F. Ding, Q. Mou, Y. Ma, G. Pan, Y. Guo, G. Tong, C.H.J. Choi, X. Zhu, C. Zhang, A crosslinked nucleic acid nanogel for effective siRNA delivery and antitumor therapy, Angew. Chem. Int. Ed. 57 (2018) 3064–3068, https://doi.org/10.1002/anie.201711242.
[24] F. Wang, M. Xie, Y. Huang, Y. Liu, X. Liu, L. Zhu, X. Zhu, Y. Guo, C. Zhang, In situ vaccination with an injectable nucleic acid hydrogel for synergistic cancer immunotherapy, Angew. Chem. Int. Ed. 63 (2024) e202315282, https://doi.org/10.1002/anie.202315282.
[25] X. Liu, M. Ma, S. Tian, W. Wang, X. Li, "Domino" cascade reactor based on DNA hydrogel for synergistic treatment of malignant tumor, Eur. J. Med. Chem. 256 (2023) 115441, https://doi.org/10.1016/j.ejmech.2023.115441.
[26] S. Belali, A.R. Karimi, M. Hadizadeh, Cell-specific and pH-sensitive nanostructure hydrogel based on chitosan as a photosensitizer carrier for selective photodynamic therapy, Int. J. Biol. Macromol. 110 (2018) 437–448, https://doi.org/10.1016/j.ijbiomac.2017.12.169.
[27] Y. Zhao, S. Jia, H. Yuan, Y. Li, R. Qi, H. Yuan, Construction of gelatin/alginate hydrogels doped hemicyanine derivatives for photodynamic antibacterial

application, Int. J. Biol. Macromol. 261 (2024) 129209, https://doi.org/10.1016/j.ijbiomac.2024.129209.
[28] M. Qiu, C. Man, Q. Zhao, X. Yang, Y. Zhang, W. Zhang, X. Zhang, J. Irudayaraj, Y. Jiang, Nanozymes meet hydrogels: fabrication, progressive applications, and perspectives, Adv. Colloid Interf. Sci. 338 (2025) 103404, https://doi.org/10.1016/j.cis.2025.103404.
[29] Y. Sang, W. Li, H. Liu, L. Zhang, H. Wang, Z. Liu, J. Ren, X. Qu, Construction of nanozyme-hydrogel for enhanced capture and elimination of bacteria, Adv. Funct. Mater. 29 (2019) 1900518, https://doi.org/10.1002/adfm.201900518.
[30] L. Yin, K. Zhang, W. Sun, Y. Zhang, Y. Wang, J. Qin, Carboxymethylcellulose based self-healing hydrogel with coupled DOX as camptothecin loading carrier for synergetic colon cancer treatment, Int. J. Biol. Macromol. 249 (2023) 126012, https://doi.org/10.1016/j.ijbiomac.2023.126012.
[31] J. Yang, Z. Sun, Q. Dou, S. Hui, P. Zhang, R. Liu, D. Wang, S. Jiang, NIR-light-responsive chemo-photothermal hydrogel system with controlled DOX release and photothermal effect for cancer therapy, Colloids Surf. A Physicochem. Eng. Asp. 667 (2023) 131407, https://doi.org/10.1016/j.colsurfa.2023.131407.
[32] L.A.L. Fliervoet, H. Zhang, E. Van Groesen, K. Fortuin, N.J.C.B. Duin, K. Remaut, R. M. Schiffelers, W.E. Hennink, T. Vermonden, Local release of siRNA using polyplex-loaded thermosensitive hydrogels, Nanoscale 12 (2020) 10347–10360, https://doi.org/10.1039/D0NR03147J.
[33] Y. Liang, J. Zhang, C. Xu, J. Wang, W. Han, J. Yang, S. Wu, J. An, J. Liu, Z. Zhang, J. Shi, K. Zhang, Biomimetic mineralized CRISPR/Cas RNA nanoparticles for efficient tumor-specific multiplex gene diting, ACS Nano 17 (2023) 15025–15043, https://doi.org/10.1021/acsnano.3c04116.
[34] T. Yang, D. Li, Z. Luo, J. Wang, F. Xiao, Y. Xu, X. Lin, Space-confined amplification for in situ imaging of single nucleic acid and single pathogen on biological samples, Adv. Sci. 11 (2024) 2407055, https://doi.org/10.1002/advs.202407055.
[35] C. Chen, Z. Yang, X. Tang, Chemical modifications of nucleic acid drugs and their delivery systems for gene-based therapy, Med. Res. Rev. 38 (2018) 829–869, https://doi.org/10.1002/med.21479.
[36] P. Vosoughi, S.M. Naghib, B.M. Kangarshahi, M.R. Mozafari, A review of RNA nanoparticles for drug/gene/protein delivery in advanced therapies: current state and future prospects, Int. J. Biol. Macromol. 295 (2025) 139532, https://doi.org/10.1016/j.ijbiomac.2025.139532.
[37] S. Neidle, Quadruplex nucleic acids as targets for anticancer therapeutics, Nat. Rev. Chem. 1 (2017) 0041, https://doi.org/10.1038/s41570-017-0041.
[38] T. Hashimoto, R. Hussien, S. Oommen, K. Gohil, G.A. Brooks, Lactate sensitive transcription factor network in L6 cells: activation of MCT1 and mitochondrial biogenesis, FASEB J. 21 (2007) 2602–2612, https://doi.org/10.1096/fj.07-8174com.
[39] S.Y.C. Choi, H. Xue, R. Wu, L. Fazli, D. Lin, C.C. Collins, M.E. Gleave, P.W. Gout, Y. Wang, The MCT4 gene: a novel, potential target for therapy of advanced prostate cancer, Clin. Cancer Res. 22 (2016) 2721–2733, https://doi.org/10.1158/1078-0432.ccr-15-1624.
[40] B. Li, L. He, D. Zuo, W. He, Y. Wang, Y. Zhang, Y. Yuan, Mutual regulation of MiR-199a-5p and HIF-1α modulates the Warburg effect in hepatocellular carcinoma, J. Cancer 8 (6) (2017) 940–949, https://doi.org/10.7150/jca.17496.
[41] K. Yu, Glutathione-activated DNA-Au nanomachine as targeted drug delivery platform for imaging-guided combinational cancer therapy, Chem. Eng. J. 419 (2021) 129535, https://doi.org/10.1016/j.cej.2021.129535.
[42] L. Feng, B. Liu, R. Xie, D. Wang, C. Qian, W. Zhou, J. Liu, D. Jana, P. Yang, Y. Zhao, An ultrasmall $SnFe_2O_4$ nanozyme with endogenous oxygen generation and glutathione depletion for synergistic cancer therapy, Adv. Funct. Mater. 31 (2021) 2006216, https://doi.org/10.1002/adfm.202006216.
[43] O.G. Lyublinskaya, Ju.S. Ivanova, N.A. Pugovkina, I.V. Kozhukharova, Z. V. Kovaleva, A.N. Shatrova, N.D. Aksenov, V.V. Zenin, Yu.A. Kaulin, I.A. Gamaley, N.N. Nikolsky, Redox environment in stem and differentiated cells: a quantitative approach, Redox Biol. 12 (2017) 758–769, https://doi.org/10.1016/j.redox.2017.04.016.
[44] J. Huang, S. Wang, Y. Xing, W. Zhou, J. Zhang, K. Cai, Interface-hybridization-enhanced photothermal performance of polypyrrole/polydopamine heterojunctions on porous nanoparticles, Macromol. Rapid Commun. 40 (2019), https://doi.org/10.1002/marc.201900263.
[45] W. Strober, Trypan blue exclusion test of cell viability, Curr. Protoc. Immunol. 111 (2015) A3.B.1–A3.B.3, https://doi.org/10.1002/0471142735.ima03bs111.
[46] M. Chang, M. Wang, M. Wang, M. Shu, B. Ding, C. Li, M. Pang, S. Cui, Z. Hou, J. Lin, A multifunctional cascade bioreactor based on hollow-structured Cu_2MoS_4 for synergetic cancer chemo-dynamic therapy/starvation therapy/phototherapy/immunotherapy with remarkably enhanced efficacy, Adv. Mater. 31 (2019), https://doi.org/10.1002/adma.201905271.